ERDC/CRREL TR-03-3

Cold Regions Research and Engineering Laboratory

US Army Corps of Engineers®
Engineer Research and Development Center

A Statistical Micromechanical Theory of Cone Penetration in Granular Materials

Jerome B. Johnson

February 2003

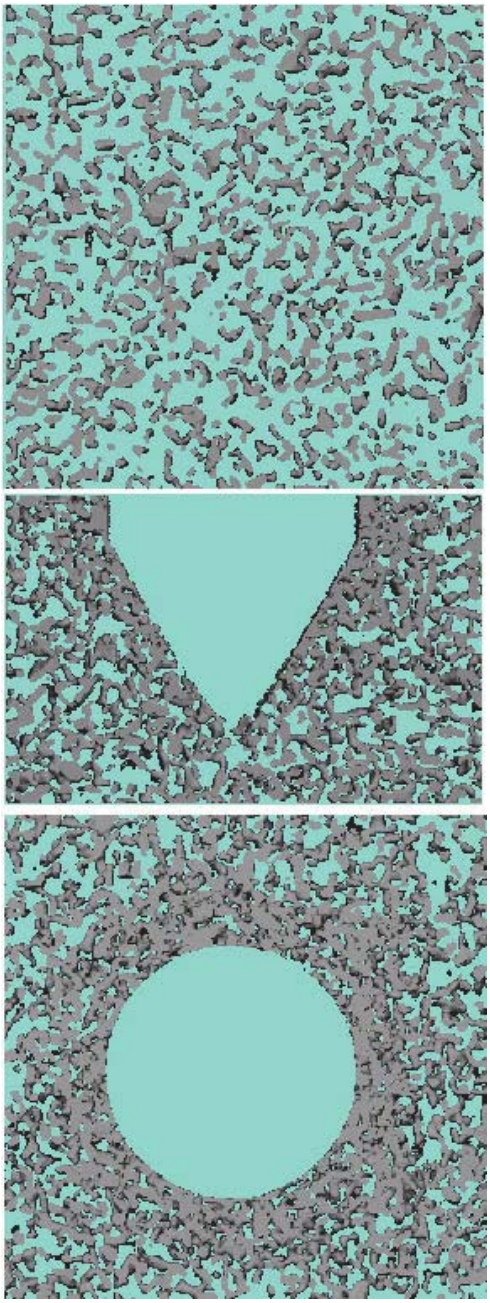

Abstract: A micromechanical theory of cone penetration in granular material is developed that takes into account the effects of soil/penetrometer friction, material compaction, and the statistics of microstructural element failure. Microstructural elements (elements) consist of particles connected to each other by cohesive or friction contacts. Soil/penetrometer friction and the deformation and failure of elements in contact with the penetrometer effective surface (PES) cause cone penetration resistance (penetration force divided by the cone base area). The PES is the interface surface between the compacted material that forms around a cone penetrometer and the surrounding elements. The cone half-angle and the volume strain at which granular particles from failed elements lock up determine the PES area. The failure of elements during penetration produces a random roughness surface of elements next to the PES. Consequently, a finite probability exists that each element next to the PES will be in contact with it at any time. The probability of contact, dimensions, and failure strength of the elements determines the percentage of elements next to the PES that contribute to penetration resistance. The statistical interaction of elements with the PES causes the maximum penetration resistance to decrease with increasing penetrometer base area, asymptotically approaching the average value. The effects of decreasing soil/penetrometer friction and the increasing PES area as a function of cone half-angle produce a minimum penetration resistance at a cone half-angle of about 15°. Element failure strength is described in terms of elastic-brittle and Mohr–Coulomb models. The theory provides a physically based method to derive in-situ mechanical and structural information for granular materials over a range of different physical scales, reducing the need to use empirical correlation. Comparison of calculations with data shows that the theory accurately predicts the experimentally observed variation of penetration resistance caused by friction, material compaction, cone penetrometer base area, and cone half-angle.

COVER: Penetration into snow, a cohesive granular material. Undisturbed snow (top), side view of the conical deformation pattern of snow around a conical penetrometer tip (middle), and the radial compaction pattern around the penetrometer base (bottom). The base diameter of the penetrometer cone is 5 mm and the cone half-angle is 30°. Photographs by M. Schneebeli (Swiss Federal Institute for Snow and Avalanche Research).

How to get copies of ERDC technical publications:

Department of Defense personnel and contractors may order reports through the Defense Technical Information Center:

DTIC-BR SUITE 0944
8725 JOHN J KINGMAN RD
FT BELVOIR VA 22060-6218
Telephone (800) 225-3842
E-mail help@dtic.mil
msorders@dtic.mil
WWW http://www.dtic.mil/

All others may order reports through the National Technical Information Service:

NTIS
5285 PORT ROYAL RD
SPRINGFIELD VA 22161
Telephone (703) 487-4650
(703) 487-4639 (TDD for the hearing-impaired)
E-mail orders@ntis.fedworld.gov
WWW http://www.ntis.gov/index.html

For information on all aspects of the Engineer Research and Development Center, visit our World Wide Web site:

http://www.erdc.usace.army.mil

Technical Report
ERDC/CRREL TR-03-3

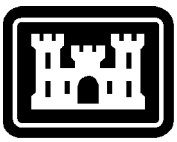

US Army Corps
of Engineers®
Engineer Research and
Development Center

A Statistical Micromechanical Theory of Cone Penetration in Granular Materials

Jerome B. Johnson

February 2003

Prepared for
OFFICE OF THE CHIEF OF ENGINEERS

PREFACE

This report was prepared by Jerome B. Johnson, Research Geophysicist, Snow and Ice Division, U.S. Army Engineer Research and Development Center (ERDC), Cold Regions Research and Engineering Laboratory (CRREL), Hanover, New Hampshire.

The work was funded by ERDC–CRREL AT24-EE-003, "Characterization of snow and other granular materials using a small-dimension penetrometer."

The author thanks D. Cole, L. Seaman, and B. Taras for their helpful comments.

CONTENTS

ILLUSTRATIONS

TABLE

NOMENCLATURE

A_b	The base area of a cone penetrometer, $A_b = \pi r_{bmax}^2$.
A_s	The penetrometer effective surface area.
c	The cohesion strength of microstructural elements for a Mohr–Coulomb failure criteria.
$f_{\perp r}$	The microstructural element failure force normal to the penetrometer surface.
$f_{\mu r}$	The force of friction between a penetrometer surface and microstructural elements or the compacted granular material (soil/penetrometer friction).
$\overline{f}_{\perp}$	The average microstructural element reaction force normal to the penetrometer surface.
f_{pr}	The component of the microstructural element failure force directed along the axis of cone penetration.
$\overline{f}_{p}$	The average microstructural element reaction force directed along the axis of cone penetration.
F_{pm}	The maximum penetration force for a cone penetrometer.
F_{β}	The influence path function that defines the influence of P_{cm2} on the total probability of contact, P_c.
$k_{\perp}$	The coefficient of elasticity normal to the penetrometer surface for a microstructural element (related to the microstructural elastic modulus by $E_{\perp} = k_{\perp} L_{\perp} / L_{\parallel}^2$).
L_1	The microstructural element average dimension along the axis of penetration.
L_2	The microstructural element average dimension normal to the axis of penetration.
$L_{\parallel}$	The microstructural element average dimension parallel to the penetrometer surface.
$L_{\perp}$	The microstructural element average dimension perpendicular to the penetrometer surface.
n	The number of failed microstructural element layers that have been traversed by the penetrometer surface (Fig. 2).

$\bar{N}_c$	The average number of microstructural elements in contact with the penetrometer effective surface.
N_{cm}	The maximum number of microstructural elements in contact with the penetrometer effective surface.
N_s	The number of microstructural elements adjacent to the penetrometer effective surface.
P	The effective normal stress acting on the failure surface of a microstructural element for the Mohr–Coulomb failure criteria.
P_c	The probability of contact for a microstructural element that is adjacent to the penetrometer effective surface.
P_{cm1}	The maximum probability of contact between microstructural elements and the penetrometer effective surface.
P_{cm2}	The added probability of contact between microstructural elements and the penetrometer effective surface due to compaction that fills the pore space of intact particles and the surface roughness of microstructural elements, Δr.
PES	Penetrometer effective surface: The cone surface or, when material compaction occurs, the interface between the compaction zone and surrounding microstructural elements (Fig. 1a and b).
R_{pm}	The maximum penetration resistance for a cone penetrometer, $R_{pm} = F_{pm}/A_b$.
r_b	The base radius of that portion of the cone penetrometer in contact with the granular material, $r_b = Z \sin\theta \cos\theta$ (Fig. 1).
r_{bmax}	The base radius for a cone penetrometer.
r_i, r_f	The radii defining the back (inner) edge, r_i, and front (outer) edge, r_f, of the compaction zone around a penetrometer (Fig. 1).
r_{imax}, r_{fmax}	The radii defining maximum values of r_i, r_f when the penetrometer is fully engaged with the granular material (Fig. 1).
r_β	The radius of the penetrometer plus the compaction zone about the penetrometer at r_b (Fig. 1).
$r_{\beta max}$	The total radius of the penetrometer plus the compaction zone around the penetrometer when it is fully engaged with the granular material (Fig. 1).

Δr	The maximum dimension of the geometric surface roughness of microstructural elements (Fig. 1b).
Z	The cone penetration depth (Fig. 1).
Z_{max}	The penetration depth at which a cone penetrometer is fully engaged with a granular material (Fig. 1a).
T_β	The thickness of the layer of compacted broken fragments or particles created by microstructural element failure (r_f–r_i).
β	The compaction volume strain of broken fragments defined as $(1 - \rho 0/\rho)$.
β_{cr}	The critical compaction coefficient defined as the compaction at which broken fragments lock up and particle rearrangement ceases.
$\delta_{\perp r}$	Microstructural element deflection at failure.
ϕ	The angle of internal friction for microstructural elements used to define the Mohr–Coulomb failure criteria.
γ, γ_{cr}	The compaction angle and critical compaction angle that defines the zone of compacted material around a cone penetrometer (Fig. 1).
μ	The coefficient of friction between the penetrometer and the compacted granular material (soil/penetrometer friction coefficient).
θ	The cone penetrometer half-angle.
ρ_0	The initial density of the granular material.
ρ	The material density in the compaction zone during compaction.
ρ_{cr}	The critical material density when a granular material locks up and further compaction through particle rearrangement no longer occurs.
τ	The shear stress on the Mohr–Coulomb failure plane between a microstructural element and its neighbors.
$\sigma^2_{N_c}$	The variance about the average number of microstructural elements in contact with the penetrometer effective surface, $\bar{N}_c$.

A Statistical Micromechanical Theory of Cone Penetration in Granular Materials

JEROME B. JOHNSON

1 INTRODUCTION

1.1 Motivation

Cone penetrometers are widely used to determine the in-situ geotechnical properties of granular materials, but difficulties arise because interpretation of penetration measurements is accomplished primarily through empirical correlation with geotechnical tests. When correlation relationships are not representative of actual soil conditions, significant interpretation errors can occur. A need exists for an accurate physically based theory that can be used to directly calculate granular material property parameters, rather than trying to compare penetration measurements with laboratory data that may not be representative of in-situ conditions. Once the validity of the theory is established it can be applied to a broad range of granular materials with a minimum of experimental verification. This stands in contrast to the extensive experimental database that is typically needed to support the empirical approach. In addition, the theory will enable us to develop scaling laws that relate the geotechnical properties determined from small-scale penetration tests to large-scale engineering problems.

1.2 Background

Most theories developed to interpret cone penetrometer resistance in granular materials are based on continuum mechanics concepts that make it difficult to account for microstructural influences. It is usually assumed that penetration through a Mohr–Coulomb elastic-plastic granular material produces a monotonically increasing pressure loading resulting in the expansion of a cavity around the penetrometer (Farrell and Greacen 1966, Greacen et al. 1968, Vesic 1972, Rohani and Baladi 1981). The shape of the expansion cavity is taken to be cylindrical for small cone angles and spherical for larger cone angles. Spherical expansion produces pressures approximately 2.4 to 3.7 times greater than those

for cylindrical expansion (Greacen et al. 1968). The effects of friction between the granular material and penetrometer are accounted for by assuming that the pressure needed to create the expansion cavity is the normal stress acting on the penetrometer face. Continuum theories predict that penetration resistance is the sum of the cavity expansion pressure and friction. The predicted penetration resistance is independent of the cone diameter, but decreases with increasing cone angle as the effects of friction decrease. However, penetrometer resistance in real granular materials varies as a function of both cone base area and cone angle, contradicting the predictions of continuum analysis.

Experiments indicate that penetration resistance can vary as a function of cone angle, with a minimum value at a cone half-angle of about $\theta = 15°$ (Gill 1968, Nowatzki and Karafiath 1972, Voorhees et al. 1975, Koolen and Vaandragen 1984). Penetration resistance has also been observed to increase as the penetrometer base area decreases (Whiteley and Dexter 1981, Bengough and Mullins 1990).

The existing experimental and numerical studies provide a good basis for understanding the micromechanics of penetration in granular materials (Gill 1968, Ashby et al. 1986, Olsen 1992, Huang et al. 1993, Gibson and Ashby 1997, Schneebeli and Johnson 1998, Johnson and Schneebeli 1999). These studies indicate that granular materials support the applied penetration forces through microstructural elements (*microstructural elements* and *elements* are used interchangeably throughout the paper) that consist of individual particles connected to each other by cohesive bonds or friction contacts. During penetration, an element in contact with the penetrometer deforms elastically in a direction normal to the penetrometer face until a critical deflection is reached, causing failure (Gill 1968, Huang et al. 1993, Gibson and Ashby 1997, Johnson 1999). Upon failure, microstructural fragments and granular particles are pushed in a direction normal to the penetrometer surface (Gill 1968, Huang et al. 1993) forming a compaction zone that extends from the tip of the cone to its base. When fragments and particles are displaced normal to the penetrometer surface the compaction zone will be conical (see the middle cover figure). The outer edge of the compaction zone is defined as the penetrometer effective surface (PES) (Fig. 1). Experiments and theory (Olsen 1992, Gibson and Ashby 1997) indicate that the variation of penetration resistance with cone base area may be the result of a microscale random roughness surface of microstructural elements next to the PES (Fig. 1b and c). This random roughness surface forms as protruding elements fail against the PES, leaving voids so that adjacent elements now protrude in front of their neighbors. Because the location and time of element failure against the PES is random, the roughness of the surface formed by the protruding elements is also random. Olsen's (1992) experiments using a 5-mm-

diameter semispherical penetrometer in aggregates of different coarseness (2- to 16-mm diameter), Gibson and Ashbey's (1997) indentation tests in foam, and Johnson and Schneebeli's (1999) penetration tests in snow all found that the measured force magnitude and its frequency fluctuated erratically, indications of material property heterogeneity and a random distribution of contacting elements.

In the following sections, the theory of cone penetration is developed, including both geometrical and micromechanical effects, using physical concepts derived from existing data. A parameter study is conducted to examine the importance of the proposed physical mechanisms, and calculated penetration resistance is compared to existing data to test the theory. We also discuss the theory as a scaling law that can be used to interpret penetration measurements and determine geotechnical properties at different physical scales.

2 STATISTICAL MICROMECHANICAL THEORY OF CONE PENETRATION

2.1 Assumptions and statistical formulation

The total force of cone penetration is the sum of the resistance force for each of the microstructural elements that are in contact with the PES. In order to determine the number of elements in contact with the PES and their resistance force we idealize the granular material and the penetration process as shown in Figure 1. The idealization is based on experimental observations and numerical simulations of penetration (discussed in Section 1) indicating that granular material deformation and associated forces are concentrated in a region immediately next to the penetrometer. The domain of the idealized granular material is the zone of compacted fragments or particles next to the penetrometer and the layer of microstructural elements next to the PES that deflect and fail during penetration (Fig. 1b and 1c). Microstructural elements outside the domain of analysis provide support to the elements next to the PES. They otherwise do not enter into the analysis since penetration forces are controlled by the deflection and failure of elements against the PES, and deformation in the bulk granular material will be small (Fig. 1a). The cone geometric parameters and the geometry of compacted and intact elements are shown in a right-half plan view from the cone centerline (Fig. 1a). A detailed view near the cone tip is shown in Figure 1b along with the force vectors from elements in contact with the penetrometer surface or PES. The idealized physical model used to develop the cone penetration theory is shown in Figure 1c. The physical model is based on the following assumptions:

1. The cone geometry is defined by its half-angle, θ, and base radius, r_{bmax} (Fig. 1a).
2. All of the elements that make up the granular material have the same dimension, elastic deformation constant, and failure strength.
3. The elements adjacent to the PES are randomly distributed (Fig. 1c).
4. The elements in contact with the PES deform elastically in a direction normal to the penetrometer surface until their force reaches a failure value.
5. Fragments from failed elements compact in a direction normal to the penetrometer surface (i.e., friction or adhesion are not strong enough to drag particles along the penetrometer surface) until they lock up.

6. The thickness of the compaction zone, $r_f - r_i$, depends on the compaction volume strain of the fragments when they lock up and the conservation of mass during compaction.
7. The PES is defined as the interface between the compaction zone and the adjacent bulk elements (Fig. 1c).
8. Friction acts between the cone penetrometer and the compacted granular material (Fig. 1b).
9. Only microstructural elements in contact with the PES may fail; elements in the bulk material remain intact until they contact the PES.

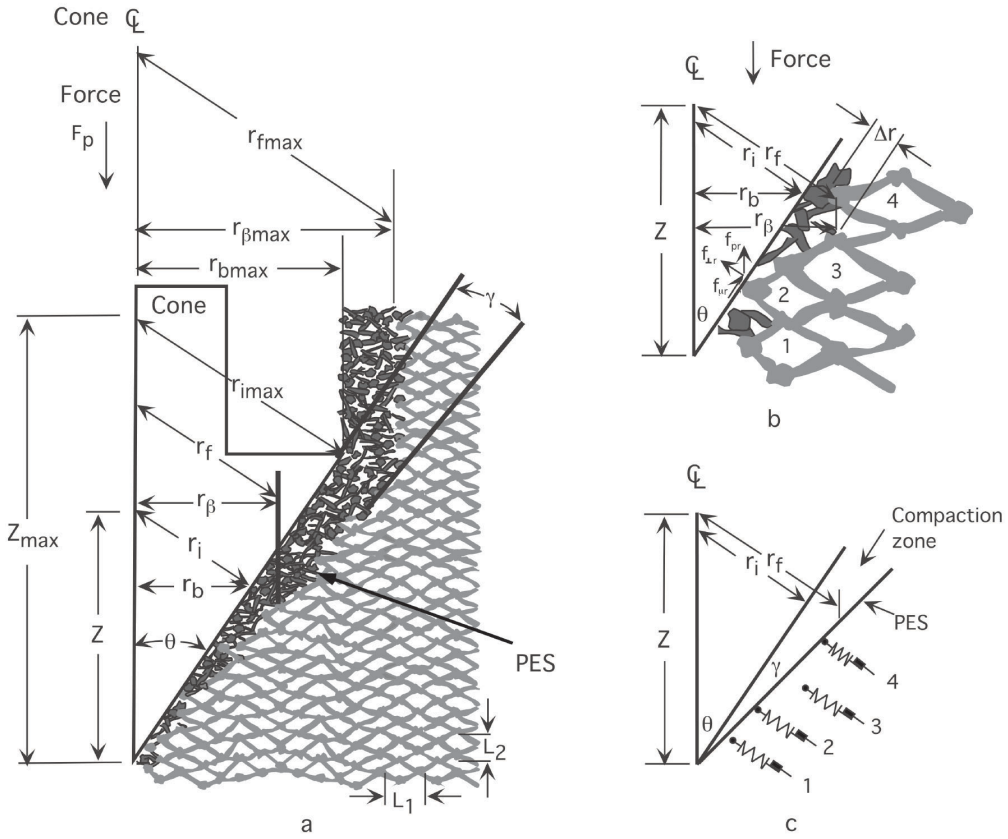

Figure 1. Granular material and penetration process. (a) Half-plan view of the geometric parameters and compaction zone for a cone penetrometer moving through a granular material. (b) Expanded view of cone tip interaction with a granular material. (c) Idealized model of cone penetrometer/granular material interaction. The spring–block objects represent randomly distributed elastic-brittle or Mohr–Coulomb elements adjacent to the PES.

Assumption 2 is a simplification of a real granular material, but is used to reduce the complexity of the statistical treatment. It is a statement that we are treating the average element properties immediately around the penetrometer. Assumption 3 introduces the statistical nature of cone penetrometer interaction with the granular material. The assumption of a random distribution of intact elements next to the PES results because the failure of elements against the PES is a random process in time and space and creates a random roughness surface of unbroken elements. Consequently, not all of the elements adjacent to the PES will be in contact with it at the same time. The maximum penetration resistance, R_{pm}, will depend on the base area of the cone, A_b. For example, when the PES equals the cross-sectional area of one element, then $R_{pm} = f_{pr}/A_b$ where f_{pr} is the force directed along the penetrometer axis when the element fails (Fig. 1b). When the PES equals the cross-sectional area of q elements then the maximum penetration resistance will be in the range $f_{pr}/(qA_b) \le R_{pm} \le f_{pr}/A_b$. The maximum penetration resistance is $f_{pr}/(qA_b)$ when the penetrometer contacts the elements separately and each element fails before the next one comes into contact (assuming the elements have no strength after failure). When the elements are in contact simultaneously and they all fail at the same time, $R_{pm} = f_{pr}/A_b$. The maximum range of possible penetration resistance values occurs when more than one element is in contact with the PES at the same time, but the elements do not fail simultaneously. For example, in Figure 1b and c, four elements are next to the PES; two of the four elements are in contact. Two of the contacting elements have different deflection amplitudes from each other so that their resistance force and time of failure will differ from each other. The total penetration resistance of the cone will depend on the micromechanical properties and statistical distribution of the elements next to the PES. Consequently, both the statistical and micromechanical aspects of the problem must be combined to successfully develop a relationship for cone penetration in granular materials.

In general, the force of cone penetration must have the form

$$F = \bar{f}_p \bar{N}_c \left(1 + m\sigma\right) \tag{1}$$

where $\bar{f}_p$ is the average resistance force directed along the penetrometer axis for elements in contact with the PES, $\bar{N}_c$ is the average number of elements in contact, and σ is the standard deviation about $\bar{N}_c$. The multiplier for the standard deviation equals zero when F equals the average penetration force and $m = 3$ when F is the maximum force of penetration. The value of m is controlled by the statistics of the problem and will be determined in Section 2.3. The terms in Equation 1 depend on the strength, dimensions, and distribution of the elements

next to the PES. They are also affected by cone geometry, material compaction, and friction between the cone and granular material.

Because of the number of physical factors that affect the penetration process, we first develop the relations describing the strength, dimensions, and compaction of the elements (Section 2.2). We next develop the statistical relations to account for the random distribution of elements next to the PES (Section 2.3) and cone geometry (Section 2.4). In Section 2.5, we combine the statistical, micromechanical, and geometric relations to give physical meaning to Equation 1 and derive the penetration resistance equation.

2.2 Microstructural element dimensions, resistance force, and compaction

Microstructural elements can be anisotropic with average dimension L_1 along the axis of penetration and average dimension L_2 perpendicular to the axis of penetration (Fig. 1a). A penetrometer, however, reacts to the element properties that are either perpendicular or parallel to its surface. Hence, we define the perpendicular and parallel element dimensions such that $L_\perp = L_1$ and $L_\parallel = L_2$ when $\theta = 90°$, and $L_\perp = L_2$ and $L_\parallel = L_1$ when $\theta = 0°$ with a smoothly varying transition for $0 < \theta < 90°$ as

$$L_\perp = \sqrt{L_1^2 \sin^2\theta + L_2^2 \cos^2\theta} \tag{2}$$

and

$$L_\parallel = \sqrt{L_1^2 \cos^2\theta + L_2^2 \sin^2\theta}\ . \tag{3}$$

The failure force for elements in contact with the PES can be treated as a yield failure condition (e.g., Mohr–Coulomb) or as a brittle rupture. The advantage of assuming a Mohr–Coulomb failure is that the effects of soil overburden or pore water pressure can be included by representing the failure as $f_{\perp r} = (c + P\tan\varphi) L_\parallel L_\perp$. The cohesion strength of the microstructural elements is c, P is the effective normal stress acting on the microstructural element failure surface, and ϕ is the internal soil friction angle. The effective area of action for the shear stress is taken to be $L_\parallel L_\perp$. For convenience, and because available data that are used in Section 3 to evaluate the theory are not affected by soil overburden or water pressure, we assume that elements fail in a brittle manner at a force of $f_{\perp r} = k_\perp \delta_{\perp r}$, where $k_\perp$ is an elastic constant and $\delta_{\perp r}$ is the element deflection at failure. Since the elements are randomly distributed

next to the PES their deflection can range from zero to $\delta_{\perp r}$ with equal probability. Consequently, the average force of the elements in contact with the PES is

$$\bar{f}_{\perp} = k_{\perp} \frac{\delta_{\perp r}}{2} = \frac{f_{\perp r}}{2}. \tag{4}$$

Microstructural element deflection, friction, and cone half-angle act on the penetrometer to produce a resistance force at failure directed along the axis of the penetrometer of

$$f_{pr} = f_{\perp r}\left(\sin\theta + \mu\cos\theta\right) \tag{5}$$

where μ is the coefficient of friction between the cone surface and granular material, and the friction force is $f_{\mu r} = \mu f_{\perp r}$ (Fig. 1b). The average resistance force, directed along the penetrometer axis, exerted by elements in contact with the PES is

$$\bar{f}_{p} = \bar{f}_{\perp}\left(\sin\theta + \mu\cos\theta\right). \tag{6}$$

Fragments or particles from broken elements are pushed in a direction normal to the penetrometer and compact as they pile up between the penetrometer and intact elements that make up the surrounding material (Fig. 1a). Compaction will continue at relatively low force until the density of the compacted material reaches a critical state where material fragments can no longer move past each other at the given applied force and they lock up. The compaction is a volume strain that describes the change in density of the material relative to its initial density and is given by

$$\beta = \left(1 - \frac{\rho_0}{\rho}\right) \tag{7}$$

where ρ_0 and ρ are the initial and current material densities, respectively. The critical (lock up) compaction coefficient is given by

$$\beta_{cr} = \left(1 - \frac{\rho_0}{\rho_{cr}}\right) \tag{8}$$

where ρ_{cr} is the critical density of compacted fragments. Mass conservation for compaction normal to the penetrometer surface requires that

$$\beta = \left(\frac{r_i}{r_f} \right)^2 \tag{9}$$

where r_i and r_f are the distances from the cone centerline axis to the cone surface and the PES, respectively (Fig. 1, Appendix A). On a microstructural scale, r_f is defined as

$$r_f = nL_\perp \tag{10}$$

where n is the number of element layers that have failed (Fig. 2).

2.3. Number of microstructural elements in contact with the PES

The random surface roughness of microstructual elements next to the PES means that not all of the elements will contact the PES at the same time (Fig. 1c). The number of elements in contact can be estimated from knowledge of the total number of elements next to the PES, their probability of contact, and an appropriate statistical distribution.

The total number of available elements next to the PES can be estimated by

$$N_s = \frac{A_s}{L_\parallel^2}. \tag{11}$$

The number of elements in contact, N_c (successes), out of the total number of elements adjacent to the PES (N_s trials) can be described by the binomial distribution with probability of contact P_c (Hays and Winkler 1971, Gibson and Ashby 1997). The average number of elements in contact and their variance are given by

$$\bar{N}_c = N_s P_c \tag{12}$$

and

$$\sigma_{N_c}^2 = N_s P_c \left(1 - P_c\right). \tag{13}$$

The maximum number of active element contacts is estimated as

$$N_{cm} = N_s P_c + 3\sqrt{N_s P_c (1 - P_c)} \tag{14}$$

where the standard deviation multiplier, 3, arises from both experimental observation and the nature of statistical distributions. Observations from indentation experiments on foam material indicate that the multiplier should equal 3 (Gibson and Ashby 1997). In addition, Tchbycheff's inequality gives the result that the probability of observing all events within three standard deviations from the mean is no less than 0.89, regardless of the distribution (Hays and Winkler 1971). The probability of observing all possible events within three standard deviations of the mean increases to 0.99 for moderately large N_s and when P_c is not near 0 or 1, the conditions under which the normal distribution can be used to approximate the binomial distribution. Simulations of the binomial distribution done for this work further indicate that the probability of observing all possible events within three standard deviations of the mean remains about 0.99 as long as $P_c + 3[P_c(1–P_c)/N_s]^{1/2} \leq 1$. Hence, the selection of $m = 3$ results in a probability of no less than 0.89 that all contact events will be observed when the probability of contact is high and N_s is relatively low. Under the more common conditions experienced by penetrometers, where P_c is relatively low or N_s is large, the probability that all contact events will be observed using $m = 3$ is 0.99.

The probability of contact, P_c, can be defined two different ways depending on how element layers fail and compact. Gibson and Ashby (1997) define the probability of contact as the constant ratio of the element deflection at failure to the total length dimension of the element perpendicular to the penetrometer surface

$$P_c = \frac{\delta_{\perp r}}{L_\perp}. \tag{15}$$

However, indentation tests indicate that P_c can vary with the state of element failure and compaction next to the PES. Often, the initial failure of elements in contact will cause the whole layer next to the PES to fail as forces that had been supported by the failed elements transfer rapidly to nearby intact elements. For a cone penetrometer, the initial failure of elements occurs near the cone tip causing that part of the cone to lose contact so that P_c will equal zero. As the cone continues into the granular material the failed elements will compact and the number of elements in contact with the compaction zone interface will increase (Fig. 2). When the compaction reaches its critical value the probability of contact is a

maximum and further movement of the penetrometer produces deflection and failure of additional elements. As the penetrometer continues into the material, the thickness of the compaction zone increases, filling in the surface roughness of elements, Δr, (Fig. 1b) and further modifying the value of P_c. Hence, at the microscale, P_c may depend on the elastic deflection of elements at failure, $\delta_{\perp r}$, the relative compaction of broken fragments, β, and the dimension of the roughness that defines the surface geometry of intact structures, Δr.

Before the initial failure of elements near the cone tip, the condition of Figure 2a, $P_{c,}$ is given by

$$P_c = P_{cm1}, \qquad 0 \le r_f \le \delta_{\perp r} \tag{16}$$

where P_{cm1} is the maximum probability of contact for elements next to the PES. After the initial rupture of elements, when the fragments are compacting, the probability of contact can be represented as

$$P_c = \left(P_{cm1} + F_\beta P_{cm2}\right)\frac{\beta\left(1-\beta_{cr}\right)}{\beta_{cr}\left(1-\beta\right)} \qquad \delta_{\perp r} \le r_f \tag{17}$$

where P_{cm2} is the additional probability that may result when broken fragments fill void space within elements. The probability P_{cm2} will depend on the packing behavior of broken fragments and the degree to which fragments can penetrate into the void space of elements. Little information is available to estimate P_{cm2} and we set it to zero for our calculations, but Gibson and Ashby (1997) observe that the compressive strength of high-porosity foam increases significantly when failed fragments fill pore space, implying that under some conditions $P_{cm2} > 0$. The function F_β describes the influence path for P_{cm2} and is defined as

$$F_\beta = \begin{cases} \left[\dfrac{T_\beta}{\Delta r}\right]^2, & T_\beta \le \Delta r \\ 1, & T_\beta > \Delta r \end{cases} \tag{18}$$

where T_β is the thickness of the compaction zone, which is derived using Equation 9 and is given by

$$T_\beta = r_f - r_i = r_i\left(\frac{1}{\sqrt{\beta_{cr}}} - 1\right). \tag{19}$$

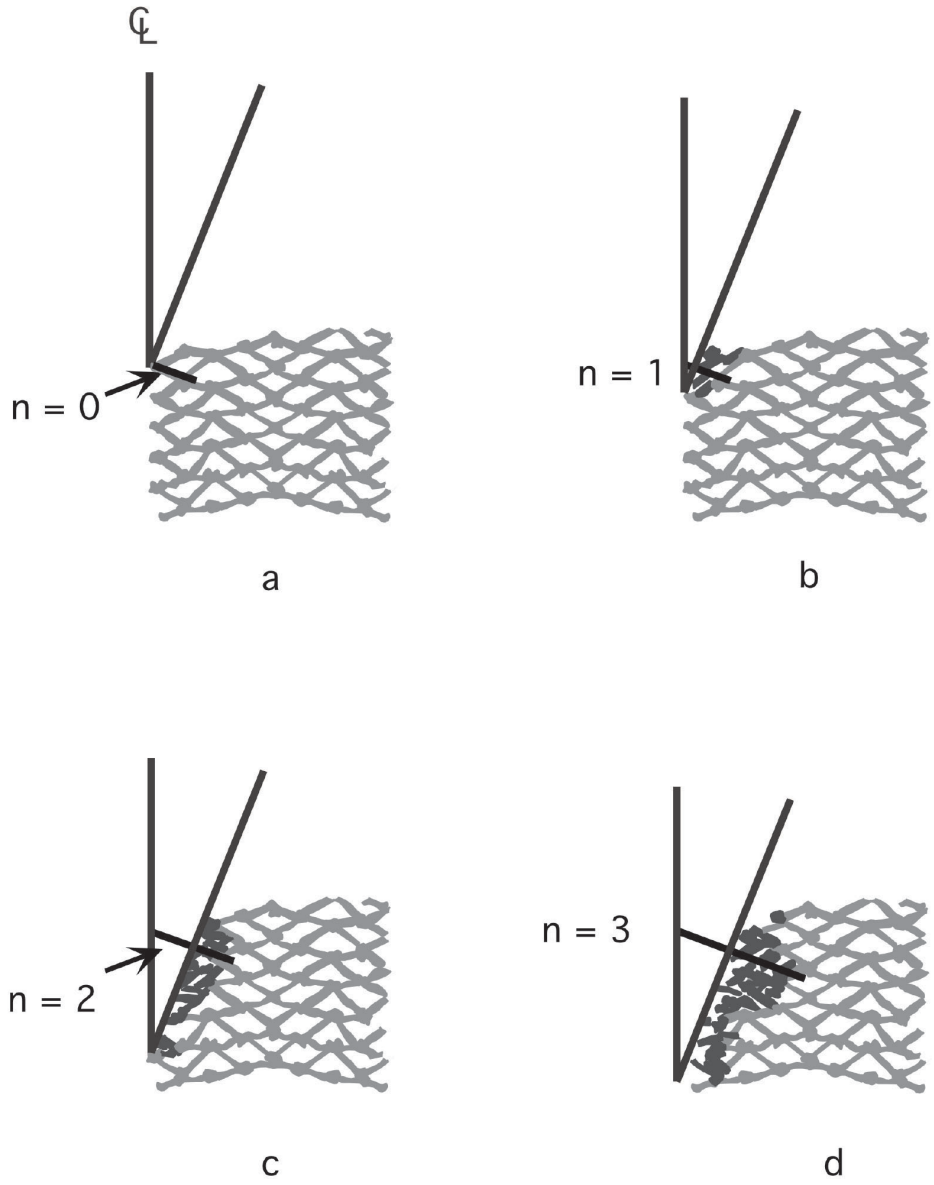

Figure 2. Progression of the zone of failed and compacted microstructural elements next to a cone penetrometer. The dark extension line perpendicular to cone surface indicates compaction length from cone centerline to PES after *n* layers have been ruptured. The number of ruptured microstructural element layers, *n*, is shown for (a) no ruptures, (b) a single layer of ruptured elements, (c) two layers of ruptured elements, and (d) three layers of ruptured elements that define the extent of the compaction zone.

2.4 Importance of cone geometry on penetration processes

The geometry of a cone penetrometer is defined by its cone half-angle, θ, and base radius, r_{bmax}. The geometry determines the magnitude of elastic and friction forces that are directed along the penetrometer's axis (Eq. 5, Fig. 1). Cone geometry also determines the shape of the compaction zone, hence, the number of elements in contact with the PES.

Penetration of a granular material begins at the cone tip with broken element fragments being pushed on a radius from the centerline axis of the penetrometer perpendicular to the penetrometer surface. The radial distance from the penetrometer centerline to the back of the compaction zone is r_i, and the radial distance to the front of the compaction zone is r_f. The radial distances to the front and back of the compaction zone vary from zero, at the cone tip, to maximums of r_{imax} and r_{fmax} at the cone base (cover figure and Fig. 1).

The radial distance to the back of the compaction zone is related to penetration depth by

$$r_i = Z \sin\theta \qquad 0 \le Z \le Z_{max} \tag{20}$$

where Z_{max} is the penetration depth at which the cone is fully engaged with the granular material and is given by

$$Z_{max} = \frac{r_{bmax}}{\sin\theta\cos\theta}. \tag{21}$$

The relationship between r_i and r_f is determined by Equation 9 and is

$$r_f = \frac{r_i}{\sqrt{\beta}} \qquad 0 \le r_i \le r_{imax} \tag{22}$$

where β is defined by Equation 7 and, when β reaches its critical value, by Equation 8 (Appendix A).

Penetration through a granular material produces a compaction zone that extends to a radius of r_β (radius of influence), at a penetration depth of Z, whose magnitude is determined by the radius of the penetrometer and the material compaction and is given by

$$r_\beta = \frac{r_b}{\sqrt{\beta}} \qquad 0 \le r_b \le r_{bmax}. \tag{23}$$

The angle of the compaction zone relative to the penetrometer surface is a function of the cone half-angle, θ, and material compaction and is

$$\gamma = \tan^{-1}\left[\tan\theta\left(\frac{1}{\sqrt{\beta}}-1\right)\right] \tag{24}$$

(Appendix A). The PES area, A_s, is

$$A_s = \frac{\pi r_{\beta max}^2}{\sin(\gamma+\theta)} = \frac{A_b}{\beta\sin(\gamma+\theta)} \tag{25}$$

and the number of elements available for contact, using Equation 11, is

$$N_s = \frac{A_s}{L_{\|}^2} = \frac{A_b}{\beta\sin(\gamma+\theta)L_{\|}^2} = \frac{\pi\sin^2\theta\cos^2\theta}{\beta\sin(\gamma+\theta)L_{\|}^2}Z_{max}^2 . \tag{26}$$

2.5 Cone penetration force and resistance

The relationships developed in the preceding sections needed to describe the statistics, micromechanics, and cone geometry that control cone penetration in granular materials can now be combined using Equation 1 to obtain equations for maximum penetration force and resistance. The statistical form for the maximum penetration force is found by substituting Equation 14 into Equation 1 to give

$$F_{pm} = \bar{f}_p N_{cm} = \bar{f}_p\left(N_s P_c + 3\sqrt{N_s P_c(1-P_c)}\right). \tag{27}$$

The physical expression for the maximum cone penetration force is obtained by substituting Equation 4 into Equation 6 and then substituting Equations 6 and 26 into Equation 27, giving

$$F_{pm} = \frac{f_{\perp r}(\sin\theta+\mu\cos\theta)A_b}{2\beta_{cr}\sin(\gamma_{cr}+\theta)L_{\|}^2}P_c\left(1+3\sqrt{\frac{\beta_{cr}\sin(\gamma_{cr}+\theta)L_{\|}^2(1-P_c)}{A_b P_c}}\right) \tag{28}$$

where β_{cr}, P_c, and γ_{cr} are defined by Equations 8, 17, and 24. Maximum penetration resistance is obtained by dividing Equation 28 by the base area of the cone:

$$R_{\mathrm{pm}} = \frac{f_{\perp \mathrm{r}}\left(\sin\theta + \mu\cos\theta\right)}{2\beta_{\mathrm{cr}}\sin\left(\gamma_{\mathrm{cr}} + \theta\right)L_{\|}^{2}} P_{\mathrm{c}} \left(1 + 3\sqrt{\frac{\beta_{cr}\sin\left(\gamma_{\mathrm{cr}} + \theta\right)L_{\|}^{2}\left(1 - P_{\mathrm{c}}\right)}{A_{\mathrm{b}}P_{\mathrm{c}}}} \right). \qquad (29)$$

The equation describing maximum penetration resistance has a complex form due to the combination of the statistical effects caused by the random roughness surface of elements next to the PES and the mechanical effects related to the failure strength of elements, compaction, and friction. The prefactors in Equations 28 and 29 are the average penetration force and resistance, respectively.

The statistical interaction of elements with the penetrometer produces a size effect described by the scaling ratio

$$S_{\mathrm{p}} = \frac{\beta_{\mathrm{cr}}\sin\left(\gamma_{\mathrm{cr}} + \theta\right)L_{\|}^{2}\left(1 - P_{\mathrm{c}}\right)}{A_{\mathrm{b}}P_{\mathrm{c}}}. \qquad (30)$$

When $S_{\mathrm{p}} >> 1$ the maximum penetration resistance is inversely proportional to $(A_{\mathrm{b}})^{-1/2}$, as observed for soil and foam (Whiteley and Dexter 1981, Gibson and Ashby 1997). When $S_{\mathrm{p}} << 1$, the maximum penetration resistance asymptotically approaches the average penetration resistance value.

2.6 Physical parameters for cone penetration in granular material

The physical parameters that determine the response characteristics of a cone penetrometer are the cone half-angle (θ), the number of microstructural elements adjacent to the PES ($N_{\mathrm{s}} = A_{\mathrm{s}}/L_{\|}^{2}$), the critical compaction coefficient (β_{cr}), soil/penetrometer friction ($\mu f_{\perp \mathrm{r}}$), the failure strength of microstructural elements ($f_{\perp \mathrm{r}}$), and the probability of contact, P_{c}, due to the random roughness surface of microstructural elements next to the PES. Figures 3 and 4 illustrate how changes in these parameters affect both the maximum and average cone penetrometer force (Eq. 28) and resistance (Eq. 29). The average penetration force and resistance is calculated using the prefactors of Equations 28 and 29, respectively.

In Figure 3, the penetration force and resistance are shown as a function of $A_{\mathrm{s}}/L_{\|}^{2}$ for a cone penetrometer from its first entry at $Z = 0$ until it is fully engaged at $Z = Z_{\max}$; the relationship between Z and the ratio $A_{\mathrm{s}}/L_{\|}^{2}$ is given by Equation 26. The compaction is defined by Equations 9 and 10 (Fig. 3c), and the force calculations were done using both a constant probability of contact, $P_{\mathrm{c}} = P_{\mathrm{cm1}}$, and a variable P_{c}, given by Equation 17 (Fig. 3d). The average penetration force and resistance calculated using a constant P_{c} are essentially identical to the average penetration force and resistance calculated using a variable P_{c} (Fig.

3a and 3b, average). However, the maximum penetration force and resistance calculated using a constant P_c differs from those calculated using a variable P_c (Fig. 3a and 3b, maximum). The maximum penetration force and resistance based on a variable P_c exhibits local maximums and minimums that correspond to the maximum and minimum values of P_c (Fig. 3d). These fluctuations decrease as a percentage of the total penetration force or resistance as $A_s/L_{\|}^2$ increases. The source of penetration force and resistance fluctuations is the failure–collapse–compaction cycle of deformation that occurs around the penetrometer. These fluctuations are significant only for small $A_s/L_{\|}^2$ ratios, which is consistent with experimental observations (Olsen 1992, Gibson and Ashby 1997, Johnson and Schneebeli 1999), indicating that the choice of using a constant or variable P_c has little effect for penetrometers with large $A_s/L_{\|}^2$ ratios.

The total magnitude of the maximum penetration resistance curve decreases as $A_s/L_{\|}^2$ increases, asymptotically approaching the average penetration resistance curve (Fig. 3a). This is the scaling effect caused by the random surface of microstructural elements next to the PES and is most pronounced when $A_s/L_{\|}^2 < 300$ (the region to the left of marker I on the top scale of Fig. 3). An effective continuum response for the penetrometer can be assumed only when the maximum and average penetration resistances are equal (at $A_s/L_{\|}^2 > 1000$, to the right of marker II, Fig. 3). The region between markers I and II is the transition between scaling dominated and continuum dominated behavior for a penetrometer.

The variation in penetrometer resistance for cones with $A_s/L_{\|}^2 > 1000$ as a function of cone angle is shown in Figure 4 for three different values of β_{cr}. A comparison of the results from Figure 4a with Figures 4b and 4c indicates that the penetration resistance at any given θ increases as β_{cr} decreases. This occurs because $A_s/L_{\|}^2$ increases as β_{cr} decreases, at a given value of θ, producing an increase in the number of microstructural elements in contact (N_c) with the PES.

For penetrometers with a high soil/penetrometer friction coefficient (Fig. 4, dashed lines), the penetration resistance starts at a relatively high value for $\theta < 15°$ and initially decreases to a minimum value and then increases again as θ increases. This response is seen in experiments (Gill 1968, Nowatzki and Karafiath 1972) and is explained by the relative partition of friction and elastic forces directed along the penetrometer axis as a function of θ (f_{pr}, Eq. 5) and on the PES area, A_s. At small values of θ the contribution to the penetration resistance from friction is relatively high. As θ increases the contribution to the penetration resistance from friction decreases while the contribution from the elastic deformation of microstructural elements and the increase in the PES area, A_s, both increase (Fig. 4). When the friction coefficient is low (Fig. 4, solid lines), the contribution from friction is small even at low θ values. Consequently,

the penetration resistance is smallest at low values of θ and then increases as the contribution from elastic deformation and A_s increase with θ.

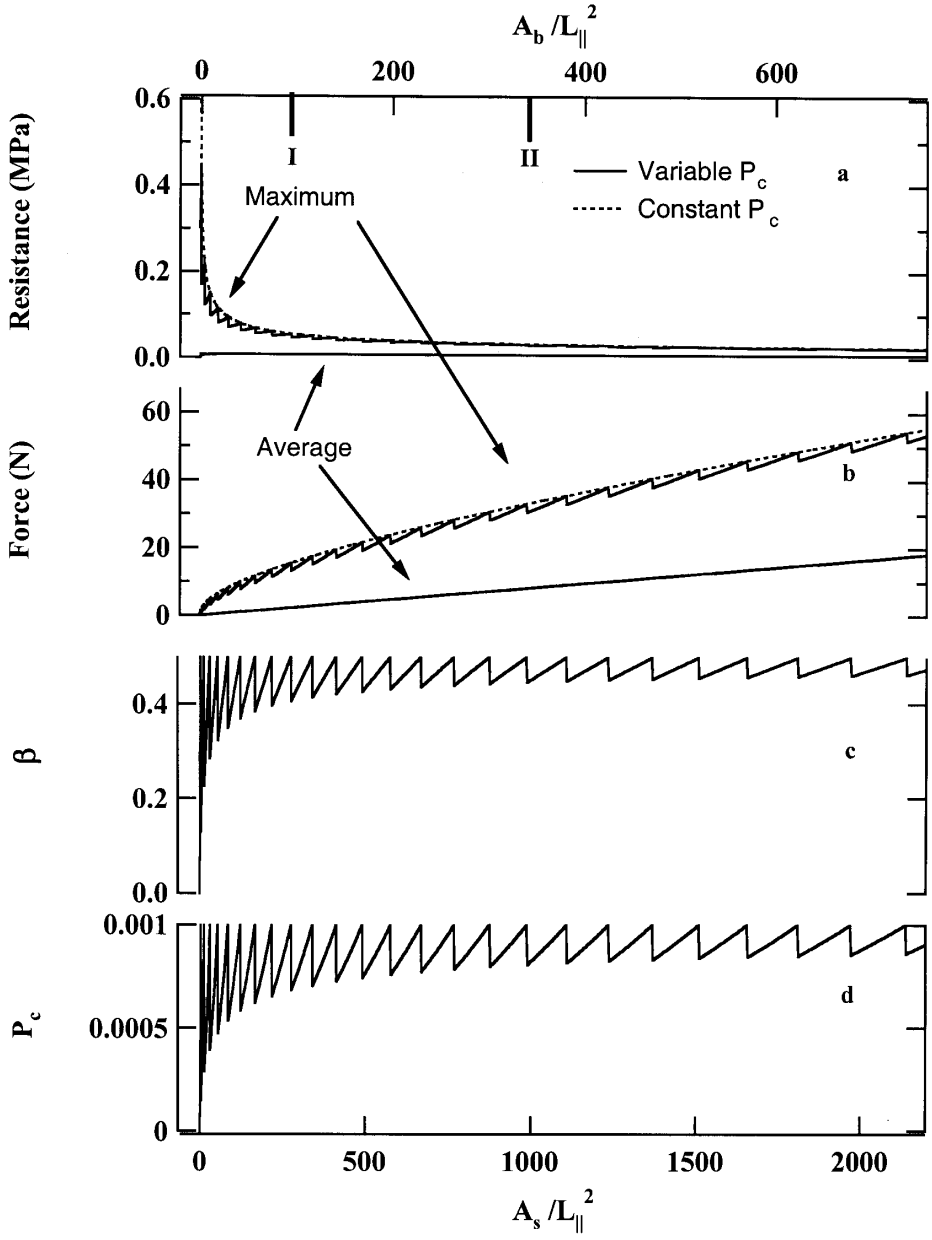

Figure 3. Penetration force and resistance as a function of $A_s/L_{||}^2$. (a) Penetration resistance, (b) penetration force, (c) material compaction, and (d) probability of contact as a function of the ratios $A_s/L_{||}^2$ and $A_b/L_{||}^2$. The material parameters are given in Table 1.

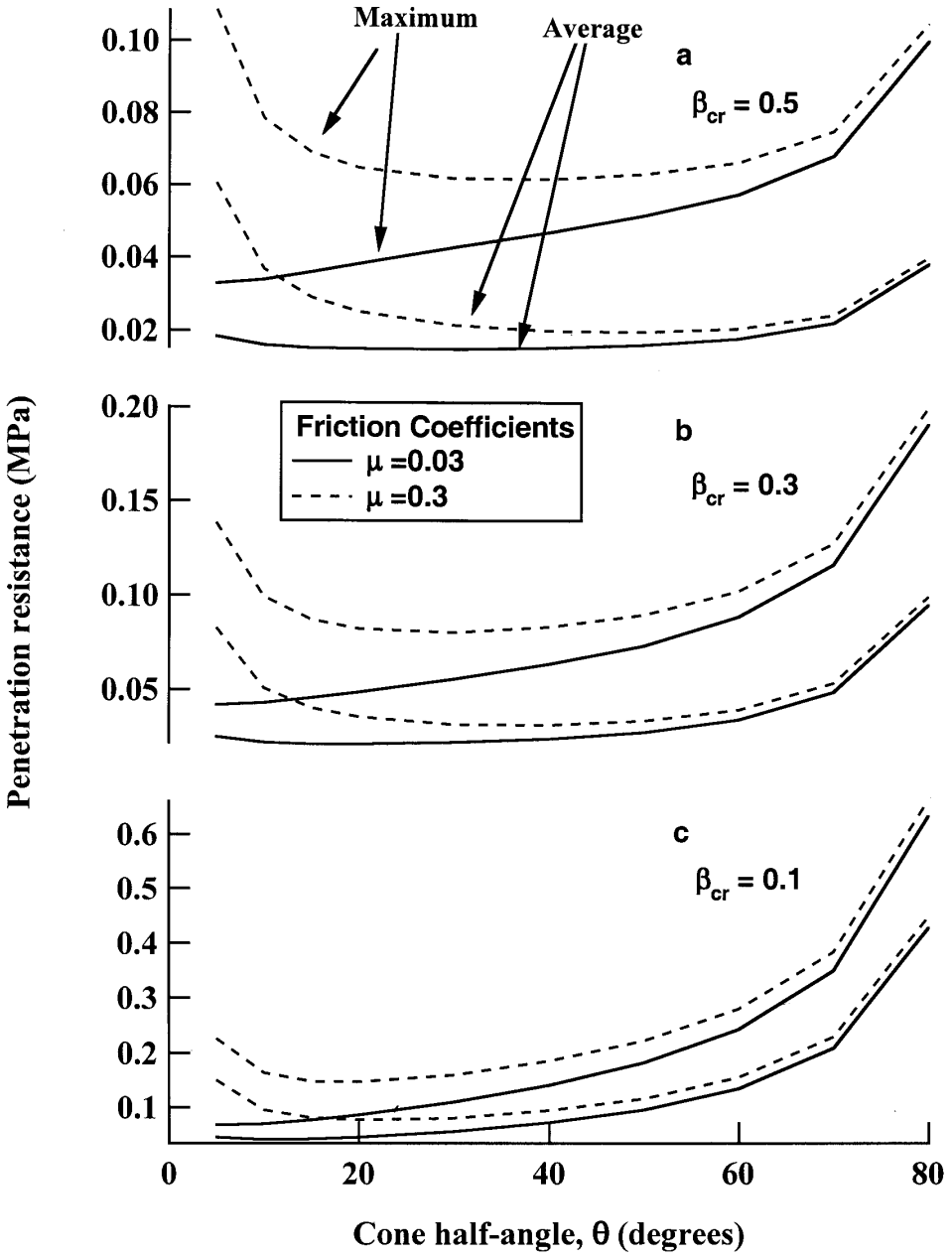

Figure 4. Penetration resistance as a function of cone angle for a penetrometer with a constant base area moving through materials with critical compaction coefficients of 0.5, 0.3, and 0.1. The material parameters are given in Table 1.

3 COMPARISON OF CALCULATED AND EXPERIMENTAL CONE PENETRATION RESISTANCE FOR SOIL

The complexity of penetrometer measurements in soil has been experimentally well documented (Gill 1968, Nowatzki and Karafiath 1972, Voorhees et al. 1975, Whiteley and Dexter 1981, Koolen and Vaandragen 1984, Ashby et al. 1986, Bengough and Mullins 1990). Results from these studies demonstrate the dependence of penetration resistance on penetrometer base area, cone half-angle, soil compaction, and friction between the penetrometer and soil, providing a rigorous test of the derived penetrometer equation (Eq. 29). Data illustrating the variation of penetration resistance for soil as a function of cone geometry (cone base area and cone half-angle), friction, and material compaction are compared to calculated maximum penetration values in Figures 5, 6, and 7.

Whitely and Dexter's (1981) tests of the dependence of penetration resistance in soil on cone base area are shown in Figure 5. In Figure 6, the results of Gill's (1968) tests using cones with different half-angle and friction coefficients are shown. In these tests, cone half-angle was varied from 3.75 to 30 degrees and the friction coefficient was changed by using bare steel and Teflon-coated steel cones. The results of Nowatzki and Karafiath (1972) are shown in Figure 7 for cone half-angles from 15° to 75° for loose, medium, and dense packed sand. In these tests, the relative degree of packing determines the β_{cr} of the sand. A loose packed sand has a larger β_{cr} than a medium packed sand, which in turn has a β_{cr} larger than dense packed sand.

Parameters used in the calculations were taken from experimental results when they were available. The values for cone half-angle used in the calculations were the same as used in the experimental tests. Friction coefficients for soil/steel were constrained between 0.2 and 0.3 based on Mohr and Karafiath's (1967) reported friction coefficient of 0.27 for sand/steel. Microstructural element failure forces, critical compaction coefficients, and soil/Teflon friction coefficients were derived using an iterative fitting process to achieve a best fit between calculated and measured penetration resistance. The soil/Teflon friction coefficients were further constrained since they were determined only after all other soil parameters had been derived using the data for the soil/steel cones (Fig. 6). The calculated failure force of the microstructural elements is between 2.5 and 22 N (Table 1). This is a similar range of force magnitude as required to displace individual aggregate particles in a bed of similar-type material (Whiteley and Dexter 1982, Olsen 1992). Microstructural element dimensions used in the calculations are less than 1 mm, which is reasonable for the soils used in this

analysis. The structural dimension is the dimension of the mechanically significant structural elements that give the soil its strength, not the grain size.

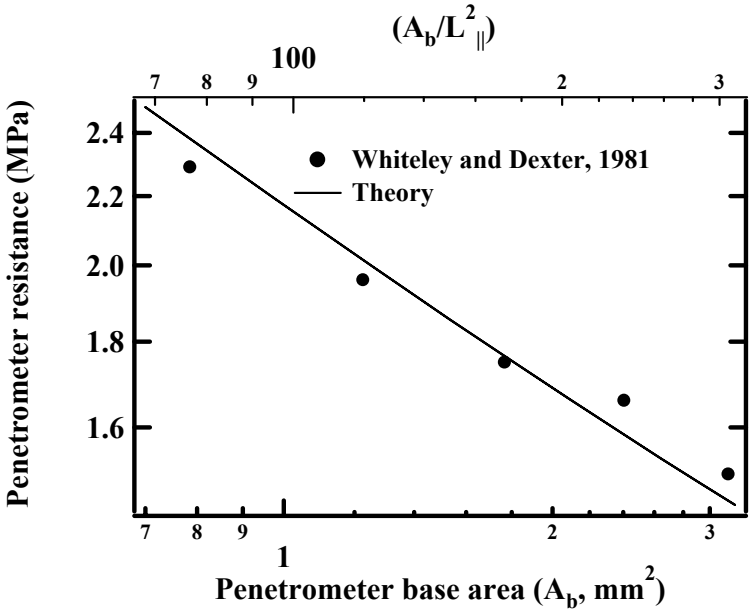

Figure 5. Comparison of calculated and measured penetration resistance as a function of penetrometer base area for Stathalbyn I soil (sandy loam over red clay; particle sizes are 26% between 2 and 0.2 mm, 44% between 0.2 and 0.02 mm, 17% between 0.02 and 0.002 mm, and 13% less than 0.002). Plot axes are logarithmic; material parameters are given in Table 1.

Even though soil parameters used in the calculations were not fully constrained by experimental data, due to a lack of available microstructural property measurements, their values fall within a narrow range that appears to be reasonable for cohesive and frictional soil (Table 1). This occurs because the cone half-angles used in the experiments are known, friction is constrained to a narrow range of values using measured data, and the parameters of the theory are directly associated with the physical processes that control penetration resistance variations. Hence, when one parameter is changed it affects the overall shape of the penetration resistance versus base area or penetration resistance versus cone half-angle curve in a unique and different way from the other physically derived parameters. Consequently, obtaining a best fit between theory and data constrains the parametric choices to a narrow range of possible values. The range of possible choices could be further restricted if more detailed measurements of penetration resistance were available (e.g., measurements of the average and variation of the penetration resistance over short time intervals).

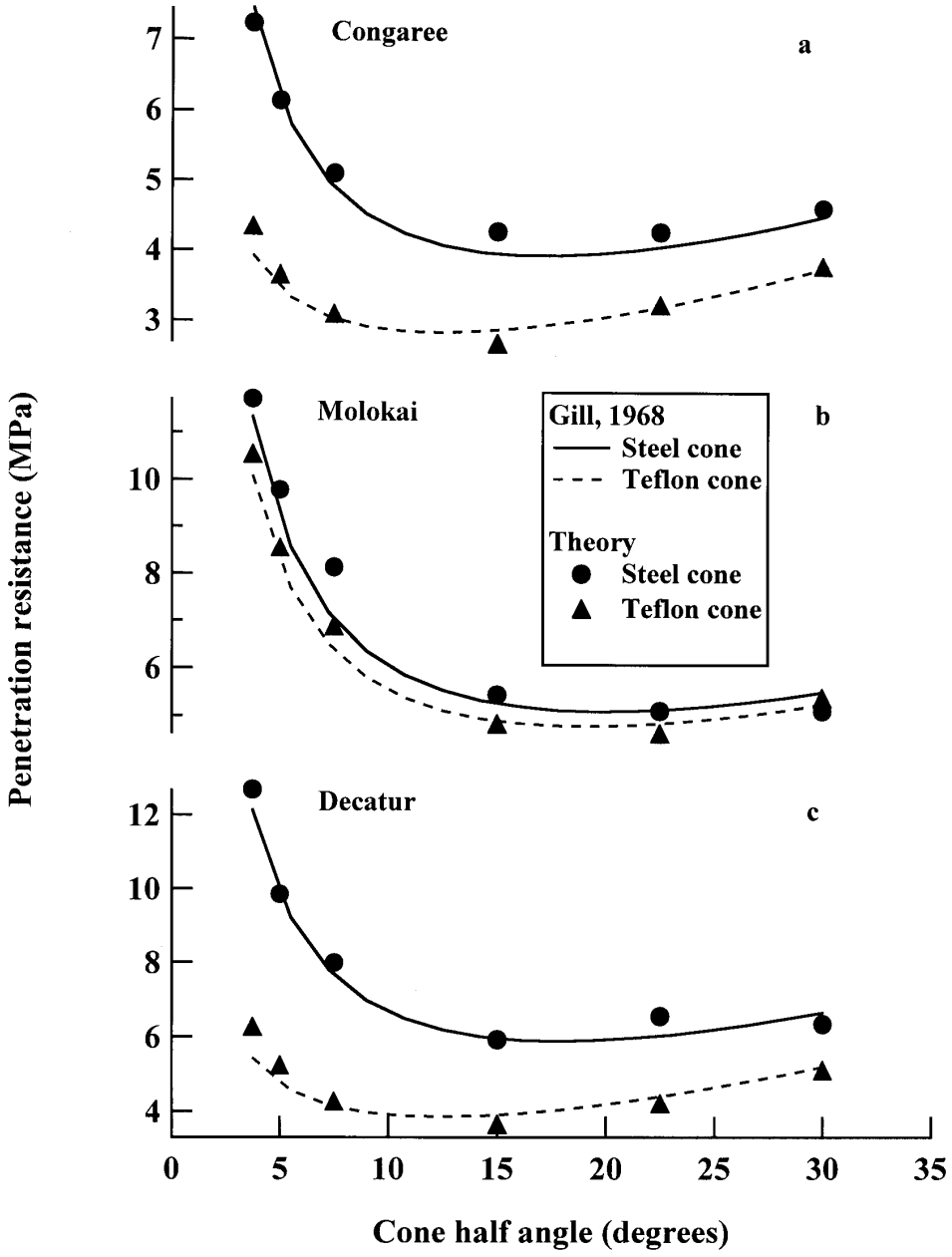

Figure 6. Comparison of calculated and measured penetration resistance as a function of cone half-angle for Congaree silty loam (28.2% moisture), Molokai silty clay (28.6% moisture), and Decatur silty clay loam (16.5% moisture). The material parameters are given in Table 1.

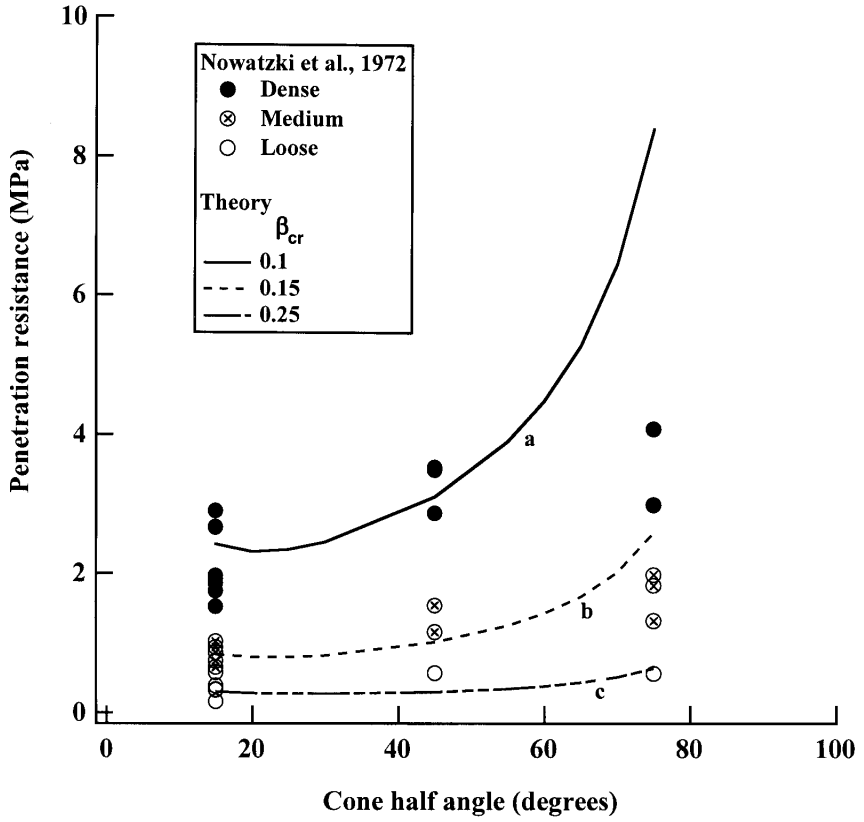

Figure 7. Comparison of calculated and measured penetration resistance as a function of cone half-angle for Jones Beach sand. The material parameters are given in Table 1.

Agreement between calculated and measured penetration resistance in Figures 5, 6, and 7 is very close, with the exception of cone half-angles greater than 50° in Figure 7. Whitely and Dexter (1981) found that the measured penetration resistance decreased as the inverse of the square root of penetrometer base area, $(A_b)^{-1/2}$; the same result was found by Ashby et al. (1986) in their experiments on zirconia foam using a flat-plate indenter. The calculated fit to Whitely and Dexter's (1981) penetration resistance data using Equation 29 has the same $(A_b)^{-1/2}$ dependence as his data and is the scaling effect caused by the random roughness surface of microstructural elements next to the PES. Also, the range of $A_s/L^2_{\|}$ values for Whitely and Dexter's data is consistent with values expected for scale-dominated effects (i.e., values less than about 300, Fig. 3, marker I).

All of the cones used to investigate the influence of varying cone angle on penetration resistance have large $A_s/L^2_{\|}$ ratios (values greater than marker II in Fig. 3). This indicates that the maximum and average penetration resistances are

essentially the same and scale effects are negligible. Consequently, variations in penetrometer resistance as a function of cone half-angle are due to friction and the variation in the PES area as a function of cone half-angle. The calculated and measured values of penetration resistance are in good agreement until the cone half-angle exceeds 45° (Fig. 6 and 7), at which point the calculated values diverge from measurements (Fig. 7). The form of the measured penetration data is the same as that shown in Figure 4. For high-friction cones, the penetration resistance is relatively high at low cone half-angle, decreases as the cone half-angle increases (Fig. 6), and then increases as the cone half-angle continues to increase (Fig. 7). For low-friction (Teflon) cones, the relative penetration resistance is low even at small cone half-angle (Fig. 6a and 6c). Cone roughness for the test results shown in Figure 6b offsets the low-friction Teflon coating (Gill 1968). The effects of friction on the penetration resistance measurements shown in Figure 6 are the same as seen in the calculated results of Figure 4 and are caused by the same mechanisms. Also, the penetration resistance magnitude and its dependence on cone half-angle decrease with increasing β_{cr} (Fig. 7, compare curves a, b, and c). This is the same behavior as was observed for the calculated results of Figure 4.

Table 1. Material parameters used for model calculations.

Fig.	A_b mm^2	θ	ρ_0 kg/m^3	β_{cr}	$L_{\parallel}L_{\perp}$ mm	$\delta_{\perp r}$ mm	$f_{\perp m}$ N	$k_{\perp}$ kN/mm	μ_s Steel/Teflon	Δr mm	P_{cm1}	P_{cm2}
3	1000	30°	250	0.5	1	0.001	22	22	0.3	0.5	0.001	0.0
4	1000	30°	*	—	1	0.001	22	22	—	0.5	0.001	0.0
5	—	30°	*	0.22	0.11	*	2.5	*	0.3	*	0.001	0.0
6a	491	—	1500	0.08	0.11	*	11.3	*	0.2/0.08	*	0.001	0.0
6b	491	—	1520	0.086	0.08	*	7.2	*	0.3/0.26	*	0.001	0.0
6c	491	—	1630	0.07	0.05	*	3	*	0.27/0.085	*	0.001	0.0
7a	323	—	1600–1700	0.1	0.09	*	4.5	*	0.3	*	0.001	0.0
7b	323	—	1500–1600	0.15	0.15	*	4.5	*	0.3	*	0.001	0.0
7c	323	—	1400–1500	0.25	0.22	*	4.5	*	0.3	*	0.001	0.0

* Parameter not needed.

— Parameter has more than one value and it is displayed on the relevant figure.

The divergence in agreement between the measured and calculated penetration resistance when cone half-angle is greater than 45° (Fig. 7) most probably occurs because the theory does not accurately describe penetration for large cone half-angles. In the theory, material compaction is in the direction normal to the cone surface irrespective of cone angle. Under these conditions, penetration

resistance will continue to increase with increasing cone half-angle as seen in the calculated results of Figures 4 and 7. However, Gill (1968) observed apparent soil bodies in front of cone penetrometers with large half-angles. These apparent soil bodies form when the shear stress in the compacted soil exceeds its shear strength, causing a shear plane failure that reduces the PES area and the maximum penetration resistance.

4 CONCLUSIONS

A statistical micromechanical theory of cone penetration in granular material was developed that takes into account the effects of cone geometry, material compaction, soil/penetrometer friction, and the dimension and strength of the microstructural elements that make up the granular material. The dependence of cone penetration resistance on cone half-angle occurs because the force contributions due to friction, microstructural element strength, and the PES area are functions of cone half-angle. Friction force contributions decrease and microstructural element elastic deformation force contributions increase with cone half-angle. In addition, as the PES area increases with cone half-angle, more microstructural elements act on the penetrometer, causing the total penetration force to increase. Consequently, penetration resistance is relatively high at small cone half-angle, decreases to a minimum value at a cone half-angle of about 15°, and then increases with cone half-angle until the compacted material around the penetrometer fails in shear, disrupting the PES.

The dependence of the maximum penetration resistance on cone base area is caused by the random surface roughness of microstructural elements next to the PES. As a result of their random distribution, not all of the microstructural elements adjacent to the PES are in contact with it at the same time. Consequently, the number of elements in contact with the PES and their force of resistance depend on the statistical probability of contact and the probability distribution of contact for elements next to the PES. When few elements are in contact with the PES, the case for a small base area penetrometer with a small PES area, the variation in penetration resistance, which is much greater than its average, determines the magnitude of the maximum penetration resistance. For a large base area penetrometer with a large PES area, many elements will contact the PES and the average penetration resistance will greatly exceed its variance, hence the maximum and average penetration resistance will be nearly the same. This statistical interaction between the elements and the PES causes the maximum penetration resistance to decrease as the penetrometer base area increases, asymptotically approaching the average value. This scaling effect can be used to determine granular material geotechnical properties at different physical scales; small-scale test measurements can be used to estimate large-scale properties needed for engineering projects. In addition, when penetration resistance measurements are made at high resolution, the force-displacement curve for individual microstructural elements can be detected; this is the variance associated with penetrometer measurements (Olsen 1992, Johnson 1999). Such measurements provide data that can be used to determine the relative element

size and strength distribution of granular materials, an important property in determining their liquefaction potential.

Predicted penetration resistance, using the penetration resistance equation and reasonable soil parameters, are in close agreement with experimental data for soils. This indicates that the theory is able to capture the complex response of a penetrometer in granular material through consideration of physical processes. The penetration equation used with high-resolution penetration resistance measurements may provide a means to directly determine geotechnical properties of granular materials, reducing the need to empirically correlate penetrometer measurements with laboratory samples that may not be representative of field conditions.

LITERATURE CITED

Ashby, M.F., A.C. Palmer, M. Thouless, D.J. Goodman, M. Howard, S.D. Hallam, S.A.F. Murrell, H. Jones, T.J.O. Sanderson, and A.R.S. Pointer (1986) Nonsimultaneous failure and ice loads on Arctic structures. In *Proceedings, 18th Annual Offshore Technology Conference (OTC), Houston, Texas, USA*, p. 399–404.

Bengough, A.G., and C.E. Mullins (1990) Mechanical impedance to root growth: A review of experimental techniques and root growth responses. *Journal of Soil Science*, **41**: 341–358.

Farrell, D.A., and E.L. Greacen (1966) Resistance to penetration of fine probes in compressible soil. *Australian Journal of Soil Research*, **4**: 1–17.

Gibson, L.J., and M.F. Ashby (1997) *Cellular solids: Structure and properties*. *Solid State Science Series*. Cambridge: Cambridge University Press, 510 p.

Gill, W.R. (1968) Influence of compaction hardening of soil on penetration resistance. *Transactions ASAE*, **11**: 741–745.

Greacen, E.L., D.A. Farrel, and B. Cockroft (1968) Soil resistance to metal probes and plant roots. In *Transactions of the 9th International Congress on Soil Science, 1*. Adelaide, Australia: Elsevier Publishing Company and International Society of Soil Science, p. 769–779.

Hays, W.L., and R.L. Winkler (1971) *Statistics: Probability, Inference, and Decision*. *Series in Quantitative Methods for Decision-Making*. New York: Holt, Rinehart and Winston, Inc., 937 p.

Huang, A.-B., M.Y. Ma, and J.S. Lee (1993) A micromechanical study of penetration tests in granular material. *Mechanics of Materials*, **16**: 133–139.

Johnson, J.B. (1999) Two-dimensional thick section penetration tests in snow. Cold Regions Research and Engineering Laboratory, Fairbanks.

Johnson, J.B., and M. Schneebeli (1999) Characterizing the microstructural and micromechanical properties of snow. *Cold Regions Science and Technology*, **30**: 91–100.

Koolen, A.J., and P. Vaandragen (1984) Relationships between soil mechanical properties. *Journal of Agricultural Engineering Research*, **29**: 313–319.

Mohr, G., and L.L. Karafiath (1967) Determination of the coefficient of friction between metals and nonmetals in ultrahigh vacuum. RE-311, Grumman Aerospace Corporation, Huntsville.

Nowatzki, E.A., and L.L. Karafiath (1972) Effect of cone angle on penetration resistance. *Highway Research Record*, **405**: 51–59.

Olsen, H.J. (1992) Sensing of aggregate by means of a horizontal mini-penetrometer. *Soil & Tillage Research*, **24**: 79–94.

Rohani, B., and G.Y. Baladi (1981) Correlation of mobility cone index with fundamental engineering properties of soil. U.S. Army Corps of Engineers Waterways Experiment Station, SL-81-4.

Schneebeli, M., and J.B. Johnson (1998) A constant-speed penetrometer for high-resolution snow stratigraphy. *Annals of Glaciology*, **26**: 107–111.

Vesic, A.S. (1972) Expansion of cavities in an infinite soil mass. *Journal of Soil Mechanics Foundation Division, Proceedings, ASCE 98*, 265–290.

Voorhees, W.B., S.A. Farrell, and W.E. Larson (1975) Soil strength and aeration effects on root elongation. *Soil Science Society of America, Proceedings*, **39**: 948–953.

Whiteley, G.M., and A.R. Dexter (1981) The dependence of soil penetrometer pressure on penetrometer size. *Journal of Agricultural Engineering Research*, **26**: 467–476.

Whiteley, G.M., and A.R. Dexter (1982) Forces required to displace individual particles within beds of similar particles. *Journal of Agricultural Engineering Research*, **27**: 215–225.

APPENDIX A. DERIVATION OF THE COMPACTION RADIUS AND COMPACTION ANGLE RELATIONSHIPS

Critical to the development of the statistical micromechanical theory of cone penetration in granular materials is the validity of the relationships that describe how the granular material compacts during the penetration process. These relationships determine the dimensions of the compaction zone and the angle of compaction during penetration of a granular material. The reference diagram for the subsequent derivations is Figure A1, which is a schematic representation of Figure 1a. The important geometric points identifying the cone geometry and compaction zone are identified by the letters A, B, C, D, E, F.

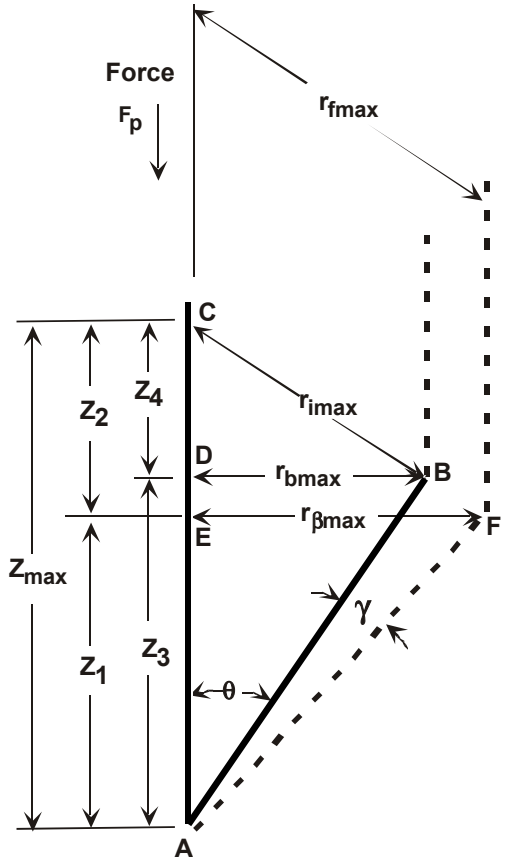

Figure A1. Schematic diagram of cone penetration in granular material. The half cone is shown by ΔABD and the compaction zone around the penetrometer by ΔAFB.

A1. Derivation of compaction radius relationships $r_{\beta max} = r_{bmax} / \sqrt{\beta}$ and $r_{fmax} = r_{imax} / \sqrt{\beta}$

The compaction radius relationships define the extent of the zone of compacted material around a penetrometer. Our derivation is based on the assumption, which is supported by experimental observation and numerical simulation (Gill 1968, Huang et al. 1993), that a cone penetrometer compacts a granular material by pushing it in a direction normal to the penetrometer surface (designated by line L_{AB}). The distance from the cone centerline axis to the back of the compaction zone is r_{imax} (along the line L_{CB}) when the cone is fully engaged with the granular material. The distance from the cone centerline axis of the cone to the front of the compaction region is r_{fmax} (along the line L_{CF}). The relationship between r_{imax} and r_{fmax} is determined by the volume compaction of the granular material from the centerline axis of the penetrometer cone out to a distance r_{fmax}. We determine the volume of compacted material and the compaction coefficient by requiring that mass of the granular material be conserved between its undisturbed and compacted state described by

$$\rho_0 V_{AFC} = \rho_f V_{AFB} \tag{A1}$$

where ρ_0 is the initial density of undisturbed material and ρ_f is the final density of compacted material. The volume of revolution for the initially undisturbed material is V_{AFC} and the volume of compacted material is V_{AFB}. The volume V_{AFC} can be represented as the sum of the two conic sections V_{AFE} and V_{FCE} giving

$$V_{AFC} = V_{AFE} + V_{FCE} = \frac{\pi}{3} r_{\beta max}^2 Z_{max} . \tag{A2}$$

The volume V_{AFB} is found by subtracting V_{ABC} from the volume V_{AFC} giving

$$V_{AFB} = V_{AFC} - V_{ABC} . \tag{A3}$$

The volume V_{AFC} is given by Equation A2 and V_{ABC} is the sum of two conic sections

$$V_{ABC} = V_{ABD} + V_{BCD} = \frac{\pi}{3} r_{bmax}^2 Z_{max} . \tag{A4}$$

Substituting Equation A4 into Equation A3 and then substituting Equations A2 and A3 into Equation A1 and rearranging gives

$$r_{\mathrm{bmax}}^2 = \left(1 - \frac{\rho_0}{\rho_\mathrm{f}}\right) r_{\beta\mathrm{max}}^2 \,. \tag{A5}$$

Taking the definition of $\beta = (1 - \rho_0/\rho_\mathrm{f})$ gives

$$r_{\beta\mathrm{max}} = \frac{r_{\mathrm{bmax}}}{\sqrt{\beta}}, \tag{A6}$$

(the same relationship applies to r_β and r_b), which is identical to Equation 23.

The compaction relationship between r_{imax} and r_{fmax} (the same relationship applies to r_i and r_f) can be derived by using the result of Equation A6 and the fact that triangles ΔBCD and ΔFCE are similar. Consequently, the ratio of the two triangles' hypotenuses equal the ratio of the length L_{BD} opposite angle ∠BCD to the length L_{EF} opposite angle ∠FCE, giving

$$\frac{r_{\mathrm{fmax}}}{r_{\beta\mathrm{max}}} = \frac{r_{\mathrm{imax}}}{r_{\mathrm{bmax}}} \,. \tag{A7}$$

Substituting Equation A6 into A7 and simplifying gives

$$r_{\mathrm{fmax}} = \frac{r_{\mathrm{imax}}}{\sqrt{\beta}}, \tag{A8}$$

which is identical to Equations 9 and 22.

A2. Derivation of the compaction angle relationship

The compaction angle, γ, is a critical parameter for the penetrometer theory as it determines the PES area. It is defined by the right triangle ΔABF where the angle ∠ABF is 90° so that the tangent of γ is given by

$$\tan\gamma = \frac{L_{\mathrm{BF}}}{L_{\mathrm{AB}}} \,. \tag{A9}$$

The dimensions of L_{BF} and L_{AB} are given by

$$L_{BF} = r_{fmax} - r_{imax} = \frac{r_{bmax}}{\cos\theta}\left(\frac{1}{\sqrt{\beta}} - 1\right) \tag{A10}$$

and

$$L_{AB} = \frac{r_{bmax}}{\sin\theta}. \tag{A11}$$

Substituting Equations A10 and A11 into A9 and rearranging gives

$$\gamma = \tan^{-1}\left[\left(\frac{1}{\sqrt{\beta}} - 1\right)\tan\theta\right]. \tag{A12}$$

REPORT DOCUMENTATION PAGE

Form Approved
OMB No. 0704-0188

1. REPORT DATE *(DD-MM-YY)*	2. REPORT TYPE	3. DATES COVERED *(From - To)*
February 2003	Technical Report	

4. TITLE AND SUBTITLE

A Statistical Micromechanical Theory of
Cone Penetration in Granular Materials

5a. CONTRACT NUMBER

5b. GRANT NUMBER

5c. PROGRAM ELEMENT NUMBER

6. AUTHOR(S)

Jerome B. Johnson

5d. PROJECT NUMBER

5e. TASK NUMBER

5f. WORK UNIT NUMBER

7. PERFORMING ORGANIZATION NAME(S) AND ADDRESS(ES)

U.S. Army Engineer Research and Development Center
Cold Regions Research and Engineering Laboratory
72 Lyme Road
Hanover, NH 03755-1290

8. PERFORMING ORGANIZATION REPORT NUMBER

ERDC/CRREL TR-03-3

9. SPONSORING/MONITORING AGENCY NAME(S) AND ADDRESS(ES)

Office of the Chief of Engineers
Washington, DC

10. SPONSOR / MONITOR'S ACRONYM(S)

11. SPONSOR / MONITOR'S REPORT NUMBER(S)

12. DISTRIBUTION / AVAILABILITY STATEMENT

Approved for public release; distribution is unlimited.

Available from NTIS, Springfield, Virginia 22161.

13. SUPPLEMENTARY NOTES

14. ABSTRACT

A micromechanical theory of cone penetration in granular material is developed that takes into account the effects of soil/penetrometer friction, material compaction, and the statistics of microstructural element failure. Microstructural elements (elements) consist of particles connected to each other by cohesive or friction contacts. Soil/penetrometer friction and the deformation and failure of elements in contact with the penetrometer effective surface (PES) cause cone penetration resistance (penetration force divided by the cone base area). The PES is the interface surface between the compacted material that forms around a cone penetrometer and the surrounding elements. The cone half-angle and the volume strain at which granular particles from failed elements lock up determine the PES area. The failure of elements during penetration produces a random roughness surface of elements next to the PES. Consequently, a finite probability exists that each element next to the PES will be in contact with it at any time. The probability of contact, dimensions, and failure strength of the elements determines the percentage of elements next to the PES that contribute to penetration resistance. The statistical interaction of elements with the PES causes the maximum penetration resistance to decrease with increasing penetrometer base area, asymptotically approaching the average value. The effects of decreasing soil/penetrometer friction and the increasing PES area as a function of cone half-angle produce a minimum penetration resistance at a cone half-angle of about 15°. Element failure strength is described in terms of elastic-brittle and Mohr–Coulomb models. The theory provides a physically based method to derive in-situ mechanical and structural information for granular materials over a range of different physical scales, reducing the need to use empirical correlation. Comparison of calculations with data shows that the theory accurately predicts the experimentally observed variation of penetration resistance caused by friction, material compaction, cone penetrometer base area, and cone half-angle.

15. SUBJECT TERMS

Cone penetrometer
Geotechnical properties
Heterogeneous granular materials
Microstructure
Scaling law
Size effects
Statistical micromechanics

16. SECURITY CLASSIFICATION OF:			17. LIMITATION OF ABSTRACT	18. NUMBER OF PAGES	19a. NAME OF RESPONSIBLE PERSON
a. REPORT	b. ABSTRACT	c. THIS PAGE			19b. TELEPHONE NUMBER *(include area code)*
U	U	U	U	43	

DEPARTMENT OF THE ARMY
ENGINEER RESEARCH AND DEVELOPMENT CENTER, CORPS OF ENGINEERS
COLD REGIONS RESEARCH AND ENGINEERING LABORATORY, 72 LYME ROAD
HANOVER, NEW HAMPSHIRE 03755-1290

Official Business